

Optimal inflow boundary condition perturbations in steady stenotic flow

X. Mao¹, H. M. Blackburn¹ and S. J. Sherwin^{2†}

¹ Department of Mechanical and Aerospace Engineering, Monash University, Vic 3800, Australia

² Department of Aeronautics, Imperial College London, South Kensington SW7 2AZ, UK

(Received 25 May 2011; revised 15 November 2011; accepted 26 January 2012;
first published online 1 March 2012)

We determine optimal inflow boundary perturbations to steady flow through a straight inflexible tube with a smooth axisymmetric stenosis at a bulk-flow Reynolds number $Re = 400$, for which the flow is asymptotically stable. The perturbations computed produce an optimal gain, i.e. kinetic energy in the domain at a given time horizon normalized by a measure of time-integrated energy on the inflow boundary segment. We demonstrate that similarly to the optimal initial condition problem, the gain can be interpreted as the leading singular value of the forward linearized operator that evolves the boundary conditions to the final state at a fixed time. In this investigation we restrict our attention to problems where the temporal profile of the perturbations examined is a product of a Gaussian bell and a sinusoid, whose frequency is selected to excite axial wavelengths similar to those of the optimal initial perturbations in the same geometry. Comparison of the final state induced by the optimal boundary perturbation with that induced by the optimal initial condition demonstrates a close agreement for the selected problem. Previous works dealing with optimal boundary perturbation considered a prescribed spatial structure and computed an optimal temporal variation of a wall-normal velocity component, whereas in this paper we consider the problem of a prescribed temporal structure and compute the optimal spatial variation of velocity boundary conditions over a one-dimensional inflow boundary segment. The methodology is capable of optimizing boundary perturbations in general non-parallel two- and three-dimensional flows.

Key words: absolute/convective instability, blood flow

1. Introduction

Incompressible flow through a smooth axisymmetric constriction in an otherwise straight rigid pipe serves as a model for physiological flow through an artery in the presence of a stenosis caused by atherosclerotic plaque. Using the justification that a diametral restriction of 50% (or 75% occlusion based on cross-sectional area) is typically both observable in ultrasound clinical investigations and taken as an indicator for surgical intervention, we concentrate on flows through a co-sinusoidal stenosis with 75% occlusion and a length which is twice the upstream pipe diameter, D , as shown in figure 1. As a result of adverse pressure gradient, flow typically separates from the

† Email address for correspondence: s.sherwin@imperial.ac.uk

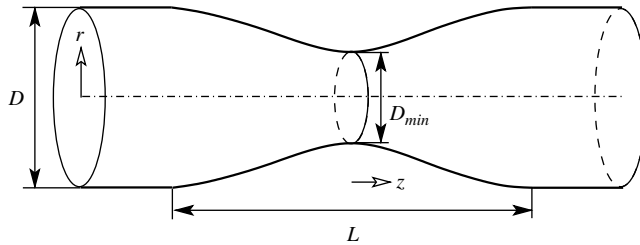


FIGURE 1. Stenosis geometry, with a co-sinusoidal shape, $L = 2D$ and $D = 2D_{min}$.

wall near the location of maximum restriction, the stenosis throat; steady laminar flow will reattach to the wall further downstream.

In this geometry, steady laminar flow of initial Hagen–Poiseuille profile becomes unstable to a Coanda-type global linear instability at Reynolds number $Re = \bar{u}D/\nu = 722$ (with \bar{u} and ν respectively the area-average inlet flow speed and fluid kinematic viscosity) that tends to make the separated jet attach to the wall some distance downstream of the stenosis throat (Sherwin & Blackburn 2005). Under nonlinear evolution, this instability saturates to a turbulent flow that reaches upstream to within approximately four diameters of the stenosis throat.

Pulsatile flow, resulting in the ejection of axisymmetric vortex rings from the stenosis throat, may also be unstable to global modes which are typically associated with these rings, and have been characterized as either taking the form of alternating tilting of successive rings, or as waves that grow within each ring (Sherwin & Blackburn 2005; Blackburn & Sherwin 2007). Using a normalizing time scale of D/\bar{u} , the pulse period T may be characterized dimensionlessly as a reduced velocity $U_{red} = \bar{u}T/D$. For simple pulse waveforms, the ring-related global instabilities occur for combinations of Reynolds numbers and reduced velocities which could be observed in the human arterial tree.

The instabilities described above are of asymptotic type, i.e. in the linear case they grow exponentially with time. However, these flows may also support very large transient energy growth of suitable initial disturbances, as a result not of asymptotic, but of local convective instability stemming from non-normality of eigenmodes (Chomaz 2005; Schmid 2007). The physics of transient growth, again for the smooth co-sinusoidal constriction, has been investigated for steady, simple pulsatile, and an example physiological waveform by Blackburn, Sherwin & Barkley (2008b) and Mao, Sherwin & Blackburn (2011). We note that these studies were carried out for Reynolds numbers which provided linear asymptotic stability, but still admit large transient growth – potentially, large enough to produce transition to turbulence for very small disturbances, i.e. bypass transition.

For steady flow at $Re = 400$, the maximum observed linear perturbation kinetic energy growth $G_{max} = G(\tau_{max}) = E(\tau_{max})/E(0) = 8.94 \times 10^4$, where $E(t)$ is volume-average kinetic energy at time t and τ_{max} is the finite time horizon which results in maximum energy growth. For steady flow at $Re = 400$, maximum growth occurs for a dimensionless time horizon $\tau_{max} = 4.40$ (times are normalized by D/\bar{u}), and occurs for a perturbation at azimuthal wavenumber $m = 1$ (Blackburn *et al.* 2008b). The optimal perturbation takes the form of a local convective instability whose dimensionless axial wavelength $\Lambda = 1.83$ (lengths are normalized by D) is preserved during the transient growth process, and the instability has the form of a sinuous disturbance to the originally axisymmetric jet shear layer. The optimal initial perturbation is concentrated

around the separation line, a feature that has also been observed for transient growth in other separating flows (Blackburn, Barkley & Sherwin 2008a; Cantwell, Barkley & Blackburn 2010). At the time horizon for maximum growth, the optimal disturbance has greatest energy density around the reattachment line of the base flow, which for $Re = 400$ is located 9.1 pipe diameters downstream of the stenosis throat.

For long-period simple (single-harmonic, non-reversing) pulsatile flow at $U_{red} = 10$, analysis presented in Blackburn *et al.* (2008b) showed that the optimal initial condition generated sinuous disturbances in an extended shear layer trailing behind the vortex ring associated with the pulse front. In many respects the optimal disturbance for that flow was similar in nature to the optimal disturbance for steady flow. Although the maximum transient energy growth for the pulsatile flow with $U_{red} = 10$, $Re = 400$ was much larger than for steady flow with the same nominal Reynolds number, i.e. $G_{max} = 1.10 \times 10^{10}$ as opposed to $G_{max} = 8.94 \times 10^4$ for steady flow, a significant proportion of the difference could be accounted for by basing the Reynolds number on the peak flow speed rather than the mean. Such a large sensitivity to Reynolds number is found in a variety of separated flows, which can exhibit exponential growth in G_{max} with Re (Cantwell *et al.* 2010). We note also that for a physiological waveform typical of that found in the human common carotid artery and which has a yet higher ratio of peak to mean flow speed than the case just described, explosive linear transient growth with $G_{max} = 1.13 \times 10^{25}$ was predicted at $Re = 300$ (Mao *et al.* 2011).

In many applications with open flows, one is potentially more interested in the possibility of transient growth brought about not by initial conditions, but by inflow boundary conditions, i.e. on perturbations which advect into the domain. For example, one may be interested in the effect of fluctuations, potentially created from upstream flow instabilities in the arterial tree or possibly respiratory and/or other external movements, on the inflow. In the past, we have studied this kind of sensitivity through direct numerical simulation (DNS) in which the inflow is perturbed with low-level uniformly distributed white noise in all velocity components (Blackburn *et al.* 2008a,b; Cantwell *et al.* 2010). In the cases studied, disturbances with maximum energy downstream of the inlet bear a very strong resemblance to the optimal disturbance at the time horizon for maximum growth.

This connection strongly suggests a direct linkage between optimal initial perturbations and optimal boundary perturbations but as yet we are only aware of boundary perturbation analysis being applied to optimal control through boundary transpiration. Motivated to investigate the inflow sensitivity of stenotic flows by T. J. Pedley (private communication), our aim in the present work is to develop a method to compute inflow perturbations of optimal gain. The methodology is based around constrained optimization obtained via maximizing a Lagrangian functional, and shares some elements with techniques previously advanced for local optimal control through wall boundary transpiration, e.g. by Corbett & Bottaro (2001) and Guégan, Schmid & Huerre (2006).

2. Problem definition

As indicated in figure 1, we adopt a cylindrical coordinate system with its origin at the centre of the stenosis throat. The (axial, radial, azimuthal) position coordinates are (z, r, θ) , and the associated components of velocity \mathbf{u} are (u, v, w) . As outlined in § 1, velocities are normalized by the bulk flow speed \bar{u} of the upstream Hagen–Poiseuille flow, and the length scale adopted is the upstream pipe diameter D , giving D/\bar{u} as the time scale, and Reynolds number $Re = \bar{u}D/\nu$. From here forward we

adopt dimensionless variables based on these normalizations. We consider a maximum Reynolds number $Re = 400$ for which the base flow is asymptotically stable; the same Reynolds number was the main focus of attention in the transient growth study of Blackburn *et al.* (2008*b*).

Working from the incompressible Navier–Stokes equations

$$\partial_t \mathbf{u} = -\mathbf{u} \cdot \nabla \mathbf{u} - \nabla p + Re^{-1} \nabla^2 \mathbf{u} \quad \text{with } \nabla \cdot \mathbf{u} = 0, \tag{2.1}$$

where p is the modified or kinematic pressure, the flow field is decomposed as the sum of a base flow and a perturbation, i.e. $(\mathbf{u}, p) = (\mathbf{U}, P) + (\mathbf{u}', p')$. The evolution of small perturbations is governed by the linearized Navier–Stokes (LNS) equations

$$\partial_t \mathbf{u}' = -\mathbf{U} \cdot \nabla \mathbf{u}' - (\nabla \mathbf{U})^T \cdot \mathbf{u}' - \nabla p' + Re^{-1} \nabla^2 \mathbf{u}' \quad \text{with } \nabla \cdot \mathbf{u}' = 0, \tag{2.2}$$

or more compactly

$$\partial_t \mathbf{u}' - L(\mathbf{u}') = 0. \tag{2.3}$$

As these equations are linear and there is a natural periodic coordinate we can further decompose the perturbation field into azimuthal Fourier modes, each of which will evolve independently. The base flow is confined to the zeroth Fourier mode. We also note that since (linearly independent) modes of forms $(\mathbf{u}', p')_m^+ = [u_m^+(z, r) \cos(m\theta), v_m^+(z, r) \cos(m\theta), w_m^+(z, r) \sin(m\theta), p_m^+(z, r) \cos(m\theta)]$ and $(\mathbf{u}', p')_m^- = [u_m^-(z, r) \sin(m\theta), v_m^-(z, r) \sin(m\theta), w_m^-(z, r) \cos(m\theta), p_m^-(z, r) \sin(m\theta)]$ retain the same forms after passage through (2.3), one can further deal with either of these reduced forms, thus effectively reducing consideration of a complex mode to a pair of real modes (Barkley & Henderson 1996). When perturbations are displayed, this is with the understanding that we will typically be dealing with $(\mathbf{u}', p')_m^\pm$. To keep notation reasonably compact in what follows we implicitly adopt Fourier decomposition for the perturbation field, only introduce its azimuthal Fourier mode index m when required, and suppress representation of θ -dependence. Here we only consider (non-axisymmetric) perturbations with $|m| > 0$, hence with zero net mass flux on any axis-normal cross-section of the domain.

This work has the aim of computing linear optimal-gain inflow boundary condition perturbations for an open flow system and in the stenotic flow under consideration these are introduced on an inflow boundary segment located two pipe diameters upstream of the stenosis throat. This is comparatively remote from the location of the energy-optimal initial perturbation, which is tightly clustered around the flow separation in the throat (Blackburn *et al.* 2008*b*), and is also sufficiently far upstream of the contraction that it is reasonable to use a Hagen–Poiseuille parabolic velocity profile on this boundary segment when computing the base flow. The initial perturbation is taken to be zero on the interior of the domain.

We let \mathbf{u}_c denote an inflow boundary velocity perturbation and assume a separation-of-variables form

$$\mathbf{u}_c(z, r, t) = \hat{\mathbf{u}}_c(z, r)f(t). \tag{2.4}$$

The objective is to optimize the spatial function $\hat{\mathbf{u}}_c(z, r)$ for a specified form of $f(t)$, in order to maximize the gain in perturbation kinetic energy at a given time horizon τ , when normalized by the kinetic energy on the boundary of $\hat{\mathbf{u}}_c(z, r)$; we will formalize this relationship in §3. Our choice of $f(t)$ is guided by prior knowledge of the form of localized convective instability in this flow (Blackburn *et al.* 2008*b*), which at $Re = 400$ is a wavepacket with axial wavelength $\Lambda = 1.83$ and an initial convection

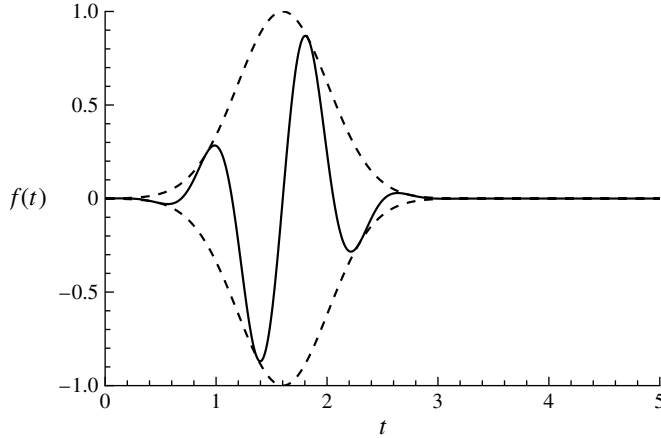


FIGURE 2. The temporal dependence of inflow boundary velocity perturbation $f(t)$ defined in (2.5). The dashed line represents the magnitude of the Gaussian term in that equation.

speed close to $U_{max} = 2\bar{u}$ (see figure 5d, Blackburn *et al.* 2008b). Also, we seek a function which has compact support in time, and thus compose the temporal variation of f as the product of a Gaussian envelope and a sinusoid:

$$f(t) = \exp(-[t - t_0]^2 / \Gamma) \cos(\omega t), \tag{2.5}$$

where $t_0 = 1.75\Lambda/U_{max} = 1.6013$ and $\Gamma = 1/3$ are adopted to make the time discontinuity at the beginning of the evolution of order of 10^{-4} and therefore approximately compatible with the (zero) initial conditions on the interior of the domain. Since the Gaussian envelope peaks at zero in the frequency domain, ω is the dominant angular frequency of $\mathbf{u}_c(z, r, t)$, and chosen based on the known wavelength Λ and the initial convection speed of the disturbance, i.e. $\omega = 4\pi\bar{u}/\Lambda \approx 6.87$. The form of $f(t)$ is illustrated in figure 2, where we observe that it has odd parity with respect to the central time of the Gaussian envelope; therefore the time integral of $f(t)$ is zero.

3. Optimization methodology

3.1. Lagrangian functional for optimal boundary conditions

We commence by introducing scalar products defined on spatial domain Ω and its boundary $\partial\Omega$:

$$(\mathbf{a}, \mathbf{b}) = \int_{\Omega} \mathbf{a} \cdot \mathbf{b} \, dV, \quad \langle \mathbf{a}, \mathbf{b} \rangle = \int_0^{\tau} \int_{\Omega} \mathbf{a} \cdot \mathbf{b} \, dV \, dt, \quad [\mathbf{c}, \mathbf{d}] = D \int_{\partial\Omega} \mathbf{c} \cdot \mathbf{d} \, dS. \tag{3.1}$$

Note the length scale D preceding the final integral, included to make ratios of the form $(\mathbf{a}, \mathbf{b})/[\mathbf{c}, \mathbf{d}]$ dimensionless. With these definitions, a Lagrangian functional for the optimal boundary condition perturbation can be expressed as

$$\mathcal{L} = \frac{(\mathbf{u}'_{\tau}, \mathbf{u}'_{\tau})}{[\hat{\mathbf{u}}_c, \hat{\mathbf{u}}_c]} - \langle \mathbf{u}^*, \partial_t \mathbf{u}' - L(\mathbf{u}') \rangle, \tag{3.2}$$

where \mathbf{u}^* is an adjoint velocity field and \mathbf{u}'_t denotes the perturbation velocity vector at time horizon $t = \tau$. The energy ratio term in this equation is what we seek to optimize,

and we denote its maximum value as the optimal gain

$$K(\tau) = \max_{\hat{u}_c} \frac{(\mathbf{u}'_\tau, \mathbf{u}'_\tau)}{[\hat{u}_c, \hat{u}_c]}, \tag{3.3}$$

while the global optimum gain, $K_{max} = \max_\tau K(\tau)$. Gain K represents the maximum possible amount of perturbation energy at time τ , normalized by a term representing the cost of the control forcing on the inflow boundary, for a specific choice of time envelope $f(t)$. The gain is determined by the spatial distribution of \hat{u}_c and is independent of its magnitude. Initial conditions in the interior of the domain are set to zero in order to make $(\mathbf{u}'_0, \mathbf{u}'_0) = 0$.

The last scalar product term in (3.2) enforces the constraint that \mathbf{u} satisfies the LNS equations. One may integrate this term by parts to obtain (Barkley, Blackburn & Sherwin 2008)

$$\begin{aligned} -\langle \mathbf{u}^*, \partial_t \mathbf{u}' - L(\mathbf{u}') \rangle &= \langle \mathbf{u}', \partial_t \mathbf{u}^* + L^*(\mathbf{u}^*) \rangle + \int_0^\tau \int_\Omega -\partial_t (\mathbf{u}' \cdot \mathbf{u}^*) \, dV \, dt \\ &+ \int_0^\tau \int_\Omega \nabla \cdot [-U(\mathbf{u}' \cdot \mathbf{u}^*) + \mathbf{u}' p^* - \mathbf{u}^* p' + Re^{-1}(\nabla \mathbf{u}' \cdot \mathbf{u}^* - \nabla \mathbf{u}^* \cdot \mathbf{u}')] \, dV \, dt, \end{aligned} \tag{3.4}$$

where $L^*(\mathbf{u}^*) = U \cdot \nabla \mathbf{u}^* - \nabla U \cdot \mathbf{u}^* - \nabla p^* + Re^{-1} \nabla^2 \mathbf{u}^*$, and $\nabla \cdot \mathbf{u}^* = 0$. Using the divergence theorem, the last integral can be stated using only boundary terms as

$$\begin{aligned} -\langle \mathbf{u}^*, \partial_t \mathbf{u}' - L(\mathbf{u}') \rangle &= \langle \mathbf{u}', \partial_t \mathbf{u}^* + L^*(\mathbf{u}^*) \rangle + \int_0^\tau \int_\Omega -\partial_t (\mathbf{u}' \cdot \mathbf{u}^*) \, dV \, dt \\ &+ \int_0^\tau \int_{\partial\Omega} \mathbf{n} \cdot [-U(\mathbf{u}' \cdot \mathbf{u}^*) + \mathbf{u}' p^* - \mathbf{u}^* p' + Re^{-1}(\nabla \mathbf{u}' \cdot \mathbf{u}^* - \nabla \mathbf{u}^* \cdot \mathbf{u}')] \, dS \, dt, \end{aligned} \tag{3.5}$$

where \mathbf{n} is a unit outward-normal vector on the boundary of the domain, $\partial\Omega$. Substituting (3.5) into (3.2), prescribing $\mathbf{u}^*(\partial\Omega) = 0$ and $\mathbf{u}'_0(\Omega) = 0$ one obtains

$$\begin{aligned} \mathcal{L} &= \frac{(\mathbf{u}'_\tau, \mathbf{u}'_\tau)}{[\hat{u}_c, \hat{u}_c]} + \langle \mathbf{u}', \partial_t \mathbf{u}^* + L^*(\mathbf{u}^*) \rangle \\ &- (\mathbf{u}^*_\tau, \mathbf{u}'_\tau) + \left[\int_0^\tau (p^* \mathbf{n} - Re^{-1} \nabla_n \mathbf{u}^*) f^*(t) \, dt, \hat{u}_c \right], \end{aligned} \tag{3.6}$$

where $\nabla_n \mathbf{u} = \mathbf{n} \cdot \nabla \mathbf{u}$ is the outward-normal component of a velocity gradient and $f^*(t)$ is the adjoint operator of $f(t)$. Considering the form of $f(t)$ defined in (2.5), we have $f^*(t) = f(t)$.

In previous work (Corbett & Bottaro 2001; Hogberg & Henningson 2002; Guégan *et al.* 2006), the pressure and a velocity component appearing in the last expression of (3.6) were eliminated as both zero-Dirichlet and zero-Neumann conditions were enforced on the boundary. In what follows we initially consider these terms to be non-zero.

Setting to zero the first variations of \mathcal{L} with respect to its independent variables \mathbf{u}^* , \mathbf{u} and \mathbf{u}_τ (\mathbf{u} and \mathbf{u}_τ are independent since their relation has been taken into account as a constraint in the definition of the Lagrangian functional) yields the following set of equations:

$$\frac{\delta \mathcal{L}}{\delta \mathbf{u}^*} = 0 \Rightarrow \partial_t \mathbf{u}' - L(\mathbf{u}') = 0, \tag{3.7}$$

$$\frac{\delta \mathcal{L}}{\delta \mathbf{u}'} = 0 \Rightarrow \partial_t \mathbf{u}^* + L^*(\mathbf{u}^*) = 0, \tag{3.8}$$

$$\frac{\delta \mathcal{L}}{\delta \mathbf{u}'_\tau} = 0 \Rightarrow \mathbf{u}^*_\tau = \frac{2\mathbf{u}'_\tau}{[\hat{\mathbf{u}}_c, \hat{\mathbf{u}}_c]}. \tag{3.9}$$

In the above, (3.7) are the LNS equations as previously defined in §2, which evolve the velocity perturbation \mathbf{u}'_0 forwards in time from $t = 0$ to $t = \tau$, (3.8) are the adjoint equations, which evolve the adjoint velocity \mathbf{u}^*_τ backwards from $t = \tau$ to $t = 0$, while (3.9) scales the outcome of the LNS equations at time $t = \tau$ in order to initialize the adjoint equation. The gradient of the Lagrangian functional with respect to the spatial distribution of the boundary condition $\hat{\mathbf{u}}_c$ can be defined as

$$\nabla_{\hat{\mathbf{u}}_c} \mathcal{L} = \frac{-2(\mathbf{u}'_\tau, \mathbf{u}'_\tau)}{[\hat{\mathbf{u}}_c, \hat{\mathbf{u}}_c]^2} \hat{\mathbf{u}}_c + \mathbf{g}(\mathbf{u}^*, p^*, \omega), \tag{3.10}$$

where

$$\mathbf{g}(\mathbf{u}^*, p^*, \omega) = \int_0^\tau (p^* \mathbf{n} - Re^{-1} \nabla_n \mathbf{u}^*) f^*(t) dt \tag{3.11}$$

is a vector function of position along the inflow boundary.

To summarize the initial and boundary conditions we adopt the following: the initial condition for the LNS equations is $\mathbf{u}'_0 = 0$ on the interior of the domain Ω . For evolution of the adjoint equations, the initial adjoint state (at time τ), \mathbf{u}^*_τ , is computed from (3.9). The domain boundary $\partial\Omega$ has four non-overlapping segments: inflow and outflow (according to the direction of the base flow), a non-slip wall, and the axis. On the inflow boundary segment of $\partial\Omega$, we have Dirichlet boundary conditions on the perturbation velocity: $\mathbf{u}' = \mathbf{u}_c = \hat{\mathbf{u}}_c f(t)$ in which the temporal function $f(t)$ is prescribed, and where the spatial function $\hat{\mathbf{u}}_c$ is part of the optimization objective. On this segment the adjoint boundary conditions are prescribed to be $\mathbf{u}^* = 0$, while for pressure variables we adopt $p' = p^* = 0$ in order to eliminate the contribution of adjoint pressure in the gradient of the Lagrangian functional in (3.10). On the outflow boundary segment, $\mathbf{u}' = \mathbf{u}^* = p' = p^* = 0$ are adopted in order that the last integral in (3.5) is zero on this segment. On the non-slip wall, zero velocities again eliminate contributions to this integral, and computed-Neumann boundary conditions are employed on pressure in a standard way for the cylindrical coordinate velocity splitting scheme (Blackburn & Sherwin 2004). Along the axis, boundary conditions depend on the azimuthal wavenumber m and solution variable, and these are zero-Dirichlet or zero-Neumann (again as outlined in Blackburn & Sherwin 2004) in combinations that also make no contribution to the same integral term.

We note that other valid combination of boundary conditions exist for the adjoint variables, i.e. the Robin condition

$$\nabla_n \mathbf{u}^* - \frac{\nabla_n \mathbf{u}'}{\mathbf{u}'} \mathbf{u}^* = 0 \quad \text{with } p^* = 0, \tag{3.12}$$

which when the perturbation flow is parallel (i.e. $\nabla_n \mathbf{u}' = 0$) is more consistent with an outflow-type boundary condition. The factor $\nabla_n \mathbf{u}' / \mathbf{u}'$ (calculated component-by-component so that each term in this ratio is scalar) is calculated and stored in the forward integration of (3.7) and substituted into the Robin condition (3.12) at every time step during the backward integration of (3.8). Careful treatment of this term is required at the intersection of this segment with the wall since at this point \mathbf{u}' is

defined to be exactly zero and so we directly enforce $\mathbf{u}' = 0$. For these boundary conditions the definition of \mathbf{g} becomes

$$\mathbf{g}(\mathbf{u}^*, p^*, \omega) = \int_0^\tau (-\mathbf{n} \cdot \mathbf{U}) \mathbf{u}' f^*(t) dt. \tag{3.13}$$

An outflow-type condition on the adjoint variable along this segment might be considered as more appropriate if one follows the heuristic argument that the ‘inflow’ boundary for the LNS equations is an ‘outflow’ boundary condition for the adjoint equations owing to the change in sign of the advection terms. We will demonstrate however that both sets of boundary conditions lead to the same value of gain. This combination of boundary conditions also requires extra memory (to store $\nabla_n \mathbf{u}' / \mathbf{u}'$) and more computer time owing to the update of the Robin condition for velocities in the backward integration. Therefore in the present work we validate the use of this type of boundary condition but have not otherwise employed it.

3.2. Eigenvalue interpretation

We denote as \mathcal{M} an evolution operator such that

$$\mathbf{u}'_\tau = \mathcal{M} \hat{\mathbf{u}}_c \quad \text{where } \mathbf{u}'_\tau \in \Omega, \hat{\mathbf{u}}_c \in \partial\Omega \tag{3.14}$$

and note that the function $f(t)$ is part of the evolution operator \mathcal{M} .

Next we introduce another operator \mathcal{M}^*

$$\mathbf{g}(\mathbf{u}^*, p^*, \omega) = \mathcal{M}^* \mathbf{u}'_\tau \quad \text{where } \mathbf{g} \in \partial\Omega, \mathbf{u}'_\tau \in \Omega, \tag{3.15}$$

whose action corresponds to first evolving \mathbf{u}'_τ backwards in the adjoint LNS equation (3.8) to obtain \mathbf{u}^* and p^* , followed by calculating \mathbf{g} from (3.11). To understand the relation between the two operators \mathcal{M} and \mathcal{M}^* , we note that when \mathbf{u}' satisfies the LNS equations and \mathbf{u}^* satisfies the adjoint equations then subject to our initial and boundary assumptions of $\mathbf{u}_0 = 0$ and $\mathbf{u}^*(\partial\Omega) = 0$, (3.5) requires that

$$(\mathbf{u}'_\tau, \mathbf{u}'_\tau) - [\hat{\mathbf{u}}_c, \mathbf{g}] = 0. \tag{3.16}$$

After substituting (3.14) and (3.15) into (3.16) we observe that \mathcal{M} and \mathcal{M}^* satisfy the duality relation

$$(\mathcal{M} \mathbf{a}, \mathbf{b}) = [\mathbf{a}, \mathcal{M}^* \mathbf{b}]. \tag{3.17}$$

We further observe, recalling (3.9), that the joint action of \mathcal{M}^* and \mathcal{M} on the boundary perturbation $\hat{\mathbf{u}}_c$ can be expressed as

$$\mathcal{M}^* \mathcal{M} \hat{\mathbf{u}}_c = \mathcal{M}^* \mathbf{u}'_\tau = \mathbf{g}(\mathbf{u}^*, p^*, \omega) \frac{[\hat{\mathbf{u}}_c, \hat{\mathbf{u}}_c]}{2}. \tag{3.18}$$

If the matrix form of the forward operator \mathcal{M} were available, we could obtain the optimal inflow perturbation, optimal gain and optimal response from the singular-value decomposition of \mathcal{M} :

$$\mathcal{M} \mathbf{U}_i = \sigma_i \mathbf{V}_i. \tag{3.19}$$

The sets of right and left singular vectors \mathbf{U}_i and \mathbf{V}_i form two orthogonal bases, and they are normalized so that $[\mathbf{U}_i, \mathbf{U}_i] = 1$ and $(\mathbf{V}_i, \mathbf{V}_i) = 1$. The singular values σ_i are real and positive. Clearly the largest singular value is the square root of the optimal gain and the corresponding right and left singular vectors are the optimal inflow perturbation and the optimal outcome.

This singular-value decomposition approach is a direct method and only the forward operator \mathcal{M} is involved, but in general the matrix form of \mathcal{M} is not available. Therefore, in the main part of this paper commencing at §4, we will adopt an adjoint–iterative method that does not explicitly require \mathcal{M} in order to calculate the optimal gain and optimal perturbation. In the remainder of this section, we will, however, demonstrate that the optimal gain and inflow perturbation are the largest eigenvalue and the corresponding eigenvector of the joint operator $\mathcal{M}^* \mathcal{M}$.

When $\hat{\mathbf{u}}_c$ converges to the eigenvector of $\mathcal{M}^* \mathcal{M}$, we see from (3.18) that $\mathbf{g}(\mathbf{u}^*, p^*, \omega)$ is parallel to $\hat{\mathbf{u}}_c$. If we denote $\mathbf{g}(\mathbf{u}^*, p^*, \omega) = \beta \hat{\mathbf{u}}_c$, then the corresponding maximal eigenvalue of the joint operator, or the optimal gain, is $K = [\mathbf{g}, \hat{\mathbf{u}}_c]/2 = \beta[\hat{\mathbf{u}}_c, \hat{\mathbf{u}}_c]/2$. Substituting (3.14) into (3.2) and recognizing that \mathcal{M} satisfies $\partial_t \mathbf{u}' = L(\mathbf{u}')$ we obtain

$$\mathcal{L} = \frac{(\mathcal{M} \hat{\mathbf{u}}_c, \mathcal{M} \hat{\mathbf{u}}_c)}{[\hat{\mathbf{u}}_c, \hat{\mathbf{u}}_c]} = \frac{[\hat{\mathbf{u}}_c, \mathcal{M}^* \mathcal{M} \hat{\mathbf{u}}_c]}{[\hat{\mathbf{u}}_c, \hat{\mathbf{u}}_c]} \tag{3.20}$$

where we have applied (3.17) to obtain the last term. Taking the variation of the Lagrangian functional (3.20) with respect to $\hat{\mathbf{u}}_c$ produces

$$\delta \mathcal{L} = \frac{2[\delta \hat{\mathbf{u}}_c, \mathcal{M}^* \mathcal{M} \hat{\mathbf{u}}_c]}{[\hat{\mathbf{u}}_c, \hat{\mathbf{u}}_c]} - \frac{2[\hat{\mathbf{u}}_c, \mathcal{M}^* \mathcal{M} \hat{\mathbf{u}}_c][\delta \hat{\mathbf{u}}_c, \hat{\mathbf{u}}_c]}{[\hat{\mathbf{u}}_c, \hat{\mathbf{u}}_c]^2}. \tag{3.21}$$

Since the joint operator $\mathcal{M}^* \mathcal{M}$ is self-adjoint, when the operator $\mathcal{M}^* \mathcal{M}$ is discretized to form an $N \times N$ matrix, then this matrix will have N real eigenvalues and N orthogonal eigenvectors. We denote the eigenvalue and eigenvector pair of this as λ_i and \mathbf{v}_i with $i = 1, \dots, N$ and $\lambda_1 \leq \lambda_2 \leq \dots \leq \lambda_N$ where \mathbf{v}_i is normalized so that $[\mathbf{v}_i, \mathbf{v}_i] = 1$.

We see that the variation of the Lagrangian functional in (3.21) is zero, at and only at, $\hat{\mathbf{u}}_c = \mathbf{v}_i$ where $\mathcal{M}^* \mathcal{M} \hat{\mathbf{v}}_i = \lambda_i \hat{\mathbf{v}}_i$. We now calculate the second-order variation to see if $\hat{\mathbf{u}}_c = \mathbf{v}_i$ are local or global extreme points of the Lagrangian functional:

$$\begin{aligned} \delta^2 \mathcal{L} = & -\frac{2[\hat{\mathbf{u}}_c, \mathcal{M}^* \mathcal{M} \hat{\mathbf{u}}_c][\delta \hat{\mathbf{u}}_c, \delta \hat{\mathbf{u}}_c]}{[\hat{\mathbf{u}}_c, \hat{\mathbf{u}}_c]^2} - \frac{8[\delta \hat{\mathbf{u}}_c, \mathcal{M}^* \mathcal{M} \hat{\mathbf{u}}_c][\hat{\mathbf{u}}_c, \delta \hat{\mathbf{u}}_c]}{[\hat{\mathbf{u}}_c, \hat{\mathbf{u}}_c]^2} \\ & + \frac{2[\delta \hat{\mathbf{u}}_c, \mathcal{M}^* \mathcal{M} \delta \hat{\mathbf{u}}_c]}{[\hat{\mathbf{u}}_c, \hat{\mathbf{u}}_c]} + \frac{8[\hat{\mathbf{u}}_c, \mathcal{M}^* \mathcal{M} \hat{\mathbf{u}}_c][\delta \hat{\mathbf{u}}_c, \hat{\mathbf{u}}_c]^2}{[\hat{\mathbf{u}}_c, \hat{\mathbf{u}}_c]^3}. \end{aligned} \tag{3.22}$$

At the stationary points where $\hat{\mathbf{u}}_c = \mathbf{v}_i$ and the second and fourth terms are balanced, the second-order variation becomes

$$\delta^2 \mathcal{L} = \frac{2}{[\hat{\mathbf{u}}_c, \hat{\mathbf{u}}_c]}([\delta \hat{\mathbf{u}}_c, \mathcal{M}^* \mathcal{M} \delta \hat{\mathbf{u}}_c] - [\delta \hat{\mathbf{u}}_c, \delta \hat{\mathbf{u}}_c] \lambda_i). \tag{3.23}$$

We recall that the sign of the second-order variation depends on the second factor on the right-hand side of (3.23). Since the eigenvectors of $\mathcal{M}^* \mathcal{M}$, \mathbf{v}_i are orthogonal, $\delta \hat{\mathbf{u}}_c$ can be represented as

$$\delta \hat{\mathbf{u}}_c = a_1 \mathbf{v}_1 + \dots + a_i \mathbf{v}_i + \dots + a_N \mathbf{v}_N. \tag{3.24}$$

Recalling that $[\mathbf{v}_i, \mathbf{v}_i] = 1$, we have

$$[\delta \hat{\mathbf{u}}_c, \mathcal{M}^* \mathcal{M} \delta \hat{\mathbf{u}}_c] = a_1^2 \lambda_1 + \dots + a_i^2 \lambda_i + \dots + a_N^2 \lambda_N, \tag{3.25}$$

and

$$[\delta \hat{\mathbf{u}}_c, \delta \hat{\mathbf{u}}_c] \lambda_i = (a_1^2 + \dots + a_i^2 + \dots + a_N^2) \lambda_i. \tag{3.26}$$

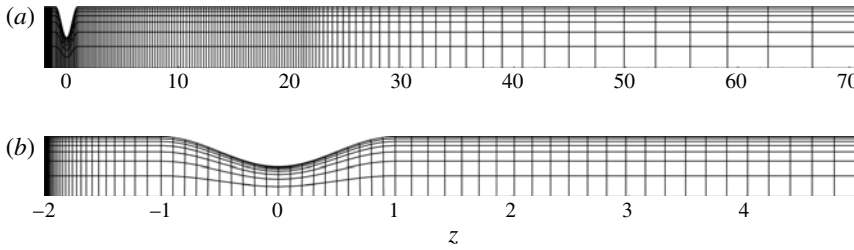


FIGURE 3. Spectral element mesh: (a) overall mesh (note use of expanded radial scale); and (b) mesh around the inflow boundary and contraction section (true aspect ratio).

Substituting (3.25) and (3.26) into (3.23), we see that if $\lambda_i = \lambda_1$, $\delta^2 \mathcal{L} \geq 0$ ($\delta^2 \mathcal{L} = 0$ is satisfied when $a_2, \dots, a_N = 0$); if $\lambda_i = \lambda_N$, $\delta^2 \mathcal{L} \leq 0$ ($\delta^2 \mathcal{L} = 0$ is satisfied when $a_1, \dots, a_{N-1} = 0$); if $\lambda_i \neq \lambda_1$ and $\lambda_i \neq \lambda_N$, the sign of $\delta^2 \mathcal{L}$ depends on the values of a_1, \dots, a_N . Therefore $\hat{\mathbf{u}}_c = \mathbf{v}_1$ is the global minimum point of the Lagrangian functional and this minimum value is λ_1 ; $\hat{\mathbf{u}}_c = \mathbf{v}_N$ is the global maximum point and this maximum value is λ_N ; $\hat{\mathbf{u}}_c = \mathbf{v}_2, \dots, \mathbf{v}_{N-1}$ are inflection points with $\delta \mathcal{L} = 0$ but are not local or global extreme points. Our optimization procedure therefore ensures that the inflow perturbation converges to the maximum value point $\hat{\mathbf{u}}_c = \mathbf{v}_N$. At this maximum point, we note that $\mathbf{g}(\mathbf{u}^*, p^*, \omega)$ is parallel with $\hat{\mathbf{u}}_c$ and the optimal gain

$$K = \lambda_N = [\mathbf{g}, \hat{\mathbf{u}}_c]/2 \quad \text{with } \mathbf{g} = \beta \hat{\mathbf{u}}_c. \tag{3.27}$$

4. Numerical methods

4.1. Discretization

Spectral elements employing piecewise continuous nodal-based polynomial expansions within mapped-quadrilateral elemental subdomains are adopted for spatial discretization of the axisymmetric geometry in the meridional semi-plane, coupled with a Fourier decomposition in azimuth. Time integration is carried out using a velocity-correction scheme. Details of the discretization and its convergence properties (exponential in spatial variables, second-order in time) are given in Blackburn & Sherwin (2004). The same numerics are used to compute base flows and the actions of the forward and adjoint LNS operators, with the same time step ($\Delta t = 1.5259 \times 10^{-4}$) being retained for all three integrations. The overall mesh and detail around the stenosis is shown in figure 3.

4.2. Optimization procedure

The optimization procedure employed to maximize the Lagrangian functional and obtain the optimal initial boundary condition, similar to the initial perturbation optimization outlined by Schmid (2007), is as follows.

- (i) Insert a random spatial function into (2.4) to generate an initial guess for \mathbf{u}_c .
- (ii) Evolve \mathbf{u}_c to obtain \mathbf{u}'_τ by integrating the LNS equations (2.3) forwards from $t = 0$ to $t = \tau$.
- (iii) Scale \mathbf{u}'_τ using (3.9) to obtain the initial condition of the adjoint equations \mathbf{u}^*_τ .
- (iv) Evolve \mathbf{u}^*_τ using (3.8) to obtain $\mathbf{g}(\mathbf{u}^*, p^*, \omega)$ by integrating the adjoint velocity field backwards from $t = \tau$ to $t = 0$.
- (v) Substitute $\mathbf{g}(\mathbf{u}^*, p^*, \omega)$ into (3.10) to obtain $\nabla_{\hat{\mathbf{u}}_c} \mathcal{L}$.

P	K (CG)	K (SG)	K (BFGS)	K (CG, Robin BC)
3	1.800	1.800	1.800	1.770
4	1.653	1.653	1.653	1.631
5	1.654	1.654	1.654	1.633
6	1.653	1.653	1.653	—
7	1.653	1.653	1.653	—

TABLE 1. Convergence of gain K with respect to spectral-element polynomial order P at $Re = 400$, $\omega = 6.87$ and $\tau = 3.0518$, as computed via various optimization algorithms (see text) and with zero Dirichlet adjoint velocity boundary conditions employed on the inflow boundary segment. The final column is calculated using the Robin boundary condition (3.12) during backward integration of the adjoint equations, while zero Dirichlet adjoint velocity boundary conditions were used to compute the other outcomes.

- (vi) Update the spatial function of the inflow perturbation from step k to $k + 1$, such that $\hat{\mathbf{u}}_c^{k+1} = \hat{\mathbf{u}}_c^k + \alpha^k \mathcal{P}(\nabla_{\hat{\mathbf{u}}_c} \mathcal{L})^k$, where α is a step length and $\mathcal{P}(\nabla_{\hat{\mathbf{u}}_c} \mathcal{L})^k$ is a search direction.
- (vii) Repeat (ii)–(vi) until the gain K converges.

The search direction $\mathcal{P}(\nabla_{\hat{\mathbf{u}}_c} \mathcal{L})$ is calculated using the Fletcher–Reeves conjugate gradient (CG) method (see e.g. Nocedal & Wright 1999). We also tested the steepest gradient (SG) and BFGS quasi-Newton methods, finding that the converged outcome is independent of choice of method. The step length α is the optimal step length obtained from a line search.

4.3. Convergence and validation

As a convergence test we consider the gain K as a function of polynomial order for CG, SG and BFGS methods as reported in table 1. We see that all the three methods converge uniformly to four significant figures at $P = 6$. The value of K is insensitive to the choice of initial boundary perturbations and if the converged optimal perturbation is polluted with a small amount of white noise and the optimization is run again with the outcome as an initial guess, the algorithm converges to the same solution. This confirms that it has reached the global maximum point of the Lagrangian function rather than a point of inflection.

The final column of table 1 shows the gain obtained using CG but with Robin boundary conditions (3.12) employed for the adjoint system on the inflow boundary segment. In this case the gain converges to within 1.5% of that obtained using the zero adjoint variable boundary conditions at an equivalent resolution. However, we have thus far been unable to make the optimization converge when using these boundary conditions with $P > 5$.

5. Results

As justified in §§ 1 and 2, in the following we set Reynolds number $Re = 400$, azimuthal wavenumber $m = 1$ and temporal frequency $\omega = 4\pi\bar{u}/\Lambda = 6.87$, if not otherwise stated. These choices provide outcomes which may be directly compared with the main body of results presented for the global optimum initial perturbation in steady stenotic flow at this Reynolds number, as described in Blackburn *et al.* (2008*b*).

Figure 4 illustrates the envelope of optimal gain for $3.05 < \tau < 14.65$, as well as two individual transient responses of optimal inflow perturbations at $\tau = 3.05$ and

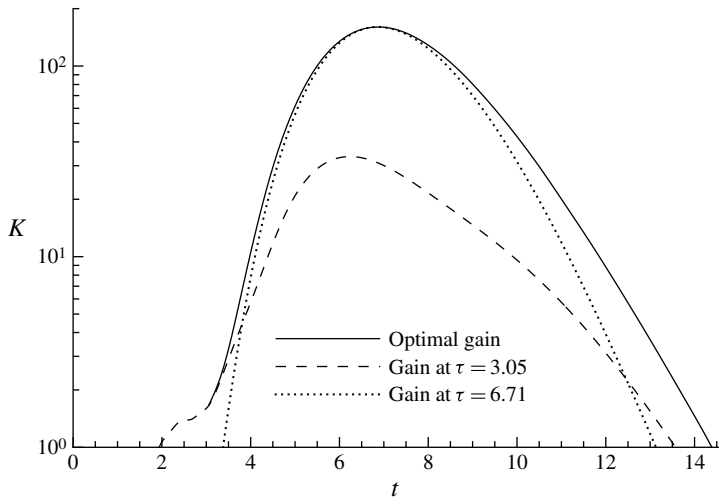


FIGURE 4. Optimal gain envelope for $Re = 400$, $m = 1$, and time evolution of transient gains with optimal inflow perturbations specific to $\tau = 3.05$ and $\tau = 6.71$; the latter is the case which provides global optimum $K_{max} = 159.4$.

$\tau = 6.71$, which in the latter case reaches the global maximum, $K_{max} = 159.4$. We do not calculate the gain from $\tau = 0$ because of the finite time required for the temporal perturbation function $f(t)$ to approach zero – as seen in figure 2 – corresponding to the time required for a disturbance to fully advect into the domain. We see that, similar to behaviour typically observed for computation of optimal initial perturbations, the curve of optimal gain is the envelope of the individual responses and it is tangent to individual evolution curves specific to each time horizon at corresponding values of τ .

Radial profiles of the three velocity components of the optimal inflow perturbations at $\tau = 3.05$ and $\tau = 6.71$ are illustrated in figure 5. The velocity profiles have been normalized such that $[\hat{u}_c, \hat{u}_c] = 1$. For perturbations in azimuthal mode $m = 1$, radial and swirl velocity components $(\hat{v}_c, \hat{w}_c)_1^+$ are equal at the axis, allowing flow to cross it. This is a consequence of the Fourier modal decompositions outlined following (2.3) and the modal decomposition of axial boundary conditions explained in Blackburn & Sherwin (2004). For $m = 1$, these axial boundary conditions also give $\hat{u}_c = 0$. All velocity components fall to zero at the wall, as required.

Figure 6(a) shows the variation of the optimal gain with Reynolds number at $\omega = 4\pi\bar{u}/\Lambda$. We see that the time horizons at which the gains reach maxima increase with Reynolds number, at least in the range investigated here. At lower Reynolds number, the stenotic flow becomes more stable (with smaller maximum transient growth, as shown in Blackburn *et al.* 2008b), and the gain reduces correspondingly. Figure 6(b) illustrates the optimal gain at other values of angular frequency ω and at fixed $\tau = 6.71$. Low frequencies ($\omega < 3$) are not considered owing to the finite width of the Gaussian function (see figure 2). We see that the angular frequency where the gain reaches a maximum is close to $\omega = 4\pi\bar{u}/\Lambda = 6$, confirming as reasonable the choice (justified in § 2) of $\omega = 6.87$ for the main body of our investigation.

The development of the global optimal inflow perturbation found with $\tau = 6.71$ is shown in figure 7. We see that at $t = 1.98$, the inflow pulse, while still not fully advected into the domain, has reached the throat, and there develops structure that is locally similar to the optimal initial condition in the shear layer adjacent to the

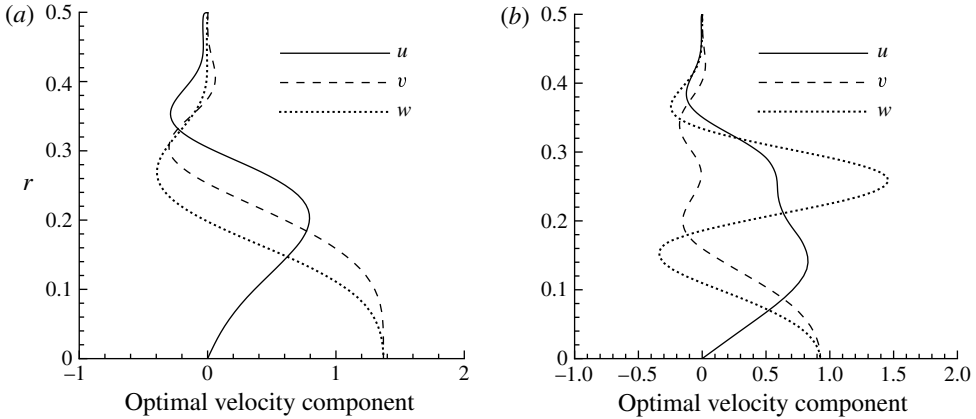


FIGURE 5. Radial profiles of optimal inflow perturbations for: (a) $\tau = 3.05$; and (b) $\tau = 6.71$.

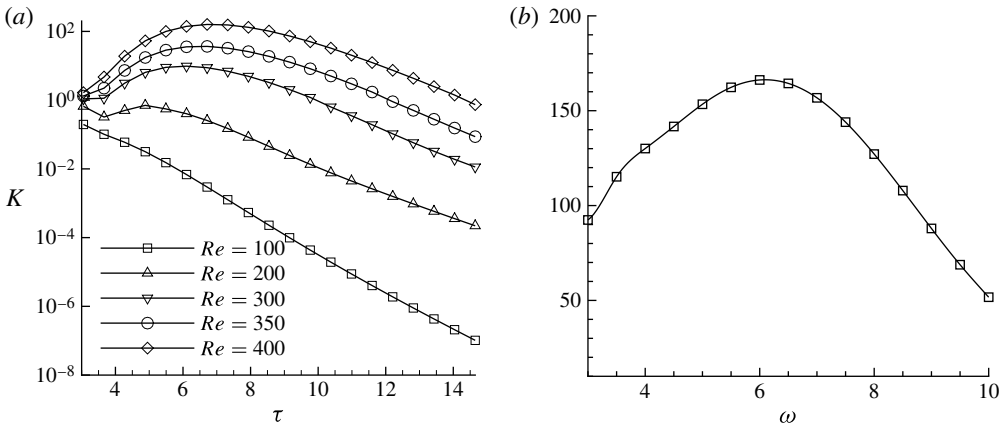


FIGURE 6. (a) Optimal gains at $Re = 100$ – 400 , $\omega = 6.87$ and (b) optimal gains for $Re = 400$, $\tau = 6.71$, $3 < \omega < 10$.

contraction throat (cf. figure 5b in Blackburn *et al.* 2008b). Figure 7(b) illustrates the response of this optimal inflow perturbation, representing the global maximum response, while figure 7(c) shows the response at a later time, illustrating that the basic structure of the perturbation is preserved as it advects downstream and weakens. The perspective view of isosurfaces of streamwise velocity shown in figure 7(d) is for $t = \tau = 6.71$, corresponding to the contours shown in figure 7(b). We note a striking similarity in both shape and axial location of the structures seen in figure 7(d) to those resulting from the optimal initial perturbation at the time for maximum energy growth, shown by a similar perspective view in figure 8(d) of Blackburn *et al.* (2008b). In both cases the optimal perturbation produces sinuous distortion of the axisymmetric shear layer present in the base flow, see also Cantwell *et al.* (2010).

Nonlinear evolution of the optimal inflow perturbation is investigated by adding the perturbation to the inflow boundary condition of the base flow and running a DNS, where the initial condition is provided by the base flow. The magnitude of the perturbation is normalized using the energy of the base flow on the inflow boundary segment, i.e. by dividing by $[U_c, U_c]^{1/2}$. The gain is computed after subtracting the

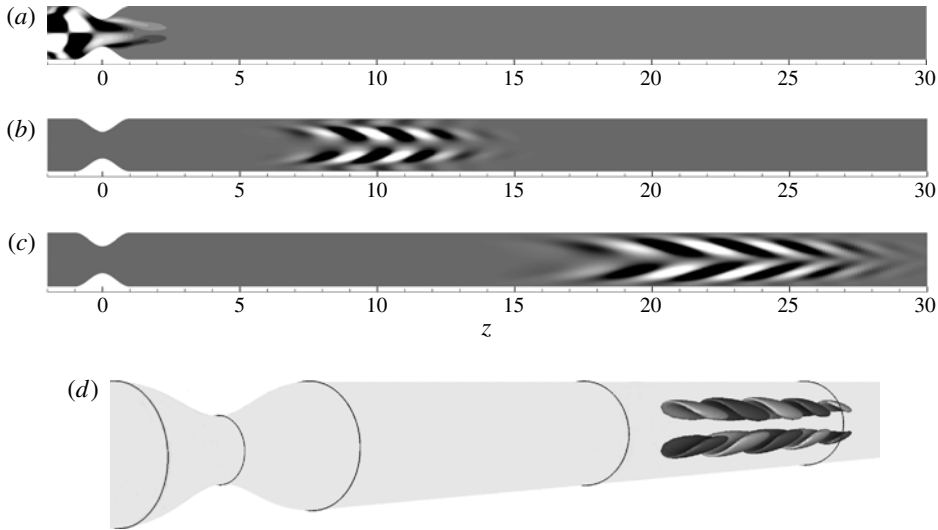


FIGURE 7. Evolution of streamwise perturbation velocity component u' produced through integrating the LNS equations when driven by the optimal boundary perturbation computed for $\tau = 6.71$, which gives the global maximum gain $K_{max} = 159.4$ in azimuthal wavenumber $m = 1$. (a–c) Contours of u' on the meridional plane for times $t = 1.98, 6.71$ (for which K_{max} is obtained) and 14.65 respectively. Contour levels are chosen arbitrarily in order to highlight the structure of perturbation flows and differ for each panel. (d) Isosurfaces of $\pm u'$ corresponding to results shown in (b), i.e. at $t = 6.71$.

base flow from the outcomes. We can observe in figure 8(a) that at small magnitude of inflow perturbations, 1×10^{-3} , the nonlinear gain agrees well with the linear gain. Using a perturbation magnitude of 1×10^{-1} leads to an earlier saturation and the gain is significantly smaller than the linear value. Interestingly an intermediate perturbation magnitude of 1×10^{-2} led to a larger gain than the 1×10^{-3} case, but in-depth investigation of this nonlinear response characteristic is beyond the scope of the present work.

Figure 8(b) illustrates the history of kinetic energy obtained via DNS in azimuthal Fourier modes other than $m = 0$. The energy of modes (integrated over the area of the domain Ω) is normalized by the energy of the unperturbed steady basic flow. The energy of the fundamental mode $m = 0$ is almost constant over the time interval considered here and is not plotted. For early times ($t < 8$), modes $m > 1$ are essentially slaved to the fundamental mode, as one expects from the Navier–Stokes equations. One may observe small-scale oscillations in energy for $m = 1$ at very early times ($t < 2$), which are associated with fluctuations in the inlet region.

6. Discussion and conclusions

A counterpart to the well-documented optimal initial value problem, the optimal boundary value problem, is investigated in this paper. An iterative optimization method is established to calculate optimal boundary perturbations as well as the optimal gain and optimal response for non-parallel flows in arbitrary geometries. It is demonstrated that the optimization method corresponds to an eigenvalue problem of the joint operator or a singular-value problem of the forward operator, indicating that the optimal gain can be also obtained via eigenvalue or singular-value decompositions

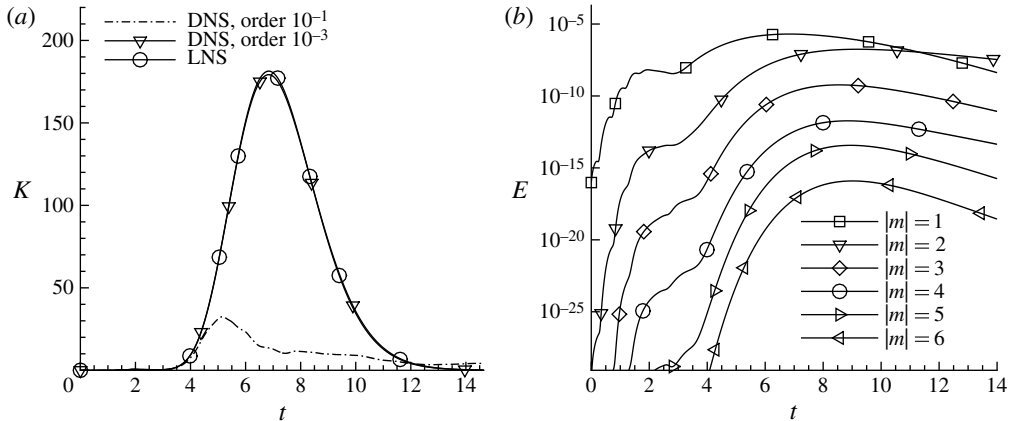


FIGURE 8. (a) The gain of the optimal boundary perturbation for the $m = 1$ mode in LNS and DNS with various magnitudes and (b) the gain of the optimal perturbation for other modes in the DNS when applying a boundary perturbation of magnitude 10^{-3} .

in locally defined problems where the matrix form of the forward operator is available after discretization. An optimization method is used to calculate the optimal inflow boundary condition perturbation of a stenotic flow. It is illustrated that the optimal inflow perturbation triggers the optimal initial perturbation and induces significant transient energy growth as the perturbation is convected downstream by the base flow. The temporal frequency at which the gain is maximized is close to the frequency of the outcome of optimal initial perturbation. We have numerically verified optimality by randomly perturbing the computed optimal boundary condition and observing that the algorithm returns to the same maximum.

We have already noted in relation to the spatial structure which develops from the optimal boundary perturbation seen in figure 7 that this bears a very strong similarity to the outcomes of optimal initial perturbation. While differences in details are to be expected, the connection between the physics of optimal boundary and initial perturbations is obviously strong, a feature we had observed in previous studies (Blackburn *et al.* 2008*a,b*; Cantwell *et al.* 2010) where in DNS we had perturbed inflows with low-amplitude white noise and observed perturbations further downstream which had strong a physical resemblance to linear optimal initial perturbation outcomes. It is also interesting to compare the time scale of the optimal gain envelope in figure 4 with that for optimal transient growth from an initial condition as shown in figure 4(a) of Blackburn *et al.* (2008*b*), where for $Re = 400$, $m = 1$, maximum growth arises for $\tau = 4.4$. In the present case, if one allows for a rise time of $t_0 = 1.60$ to reach the centroid of the Gaussian envelope in (2.5), and another interval of approximately $2D/2\bar{u} = 1$ for a boundary perturbation to advect at the peak speed of the incoming Hagen–Poiseuille flow to the zone for the optimal initial condition (the stenosis throat), there is a remaining time horizon of order $\tau \approx 6.71 - 1.6 - 1 = 4.1$. While these considerations are approximate, they are suggestive that this value is reasonably similar to the time horizon for global optimum transient growth from an initial condition. We may informally conceptualize the process of optimal boundary perturbation for these problems as being closely related to that for the optimal initial condition, whereby the boundary perturbation advects to the zone for the optimal initial condition, convolves with its distribution, and the subsequent physics is essentially that resulting from an optimal initial perturbation.

Acknowledgements

We would like to acknowledge financial support from the Australian Research Council through Discovery Program Grant DP1094851, and from Australia's National Computational Infrastructure via Merit Allocation Scheme Grant D77. S.J.S. would like to acknowledge financial support under EPSRC grant EP/H050507/1.

REFERENCES

- BARKLEY, D., BLACKBURN, H. M. & SHERWIN, S. J. 2008 Direct optimal growth analysis for timesteppers. *Intl J. Numer. Meth. Fluids* **57**, 1437–1458.
- BARKLEY, D. & HENDERSON, R. D. 1996 Three-dimensional Floquet stability analysis of the wake of a circular cylinder. *J. Fluid Mech.* **322**, 215–241.
- BLACKBURN, H. M., BARKLEY, D. & SHERWIN, S. J. 2008a Convective instability and transient growth in flow over a backward-facing step. *J. Fluid Mech.* **603**, 271–304.
- BLACKBURN, H. M. & SHERWIN, S. J. 2004 Formulation of a Galerkin spectral element–Fourier method for three-dimensional incompressible flows in cylindrical geometries. *J. Comput. Phys.* **197** (2), 759–778.
- BLACKBURN, H. M. & SHERWIN, S. J. 2007 Instability modes and transition of pulsatile stenotic flow: pulse-period dependence. *J. Fluid Mech.* **573**, 57–88.
- BLACKBURN, H. M., SHERWIN, S. J. & BARKLEY, D. 2008b Convective instability and transient growth in steady and pulsatile stenotic flows. *J. Fluid Mech.* **607**, 267–277.
- CANTWELL, C. D., BARKLEY, D. & BLACKBURN, H. M. 2010 Transient growth analysis of flow through a sudden expansion in a circular pipe. *Phys. Fluids* **22**, 034101–1–15.
- CHOMAZ, J.-M. 2005 Global instabilities in spatially developing flows: non-normality and nonlinearity. *Annu. Rev. Fluid Mech.* **37**, 357–392.
- CORBETT, P. & BOTTARO, A. 2001 Optimal control of nonmodal disturbance in boundary layers. *Theor. Comput. Fluid Dyn.* **15**, 65–81.
- GUÉGAN, A., SCHMID, P. J. & HUERRE, P. 2006 Optimal energy growth and optimal control in swept Hiemenz flow. *J. Fluid Mech.* **566**, 11–45.
- HOGBERG, M. & HENNINGSON, D. S. 2002 Linear optimal control applied to instabilities in spatially developing boundary layers. *J. Fluid Mech.* **470**, 151–179.
- MAO, X., SHERWIN, S. J. & BLACKBURN, H. M. 2011 Transient growth and bypass transition in stenotic flow with a physiological waveform. *Theor. Comput. Fluid Dyn.* **25** (1), 31–42.
- NOCEDAL, J. & WRIGHT, S. 1999 *Numerical Optimization*. Springer.
- SCHMID, P. J. 2007 Nonmodal stability theory. *Annu. Rev. Fluid Mech.* **39**, 129–162.
- SHERWIN, S. J. & BLACKBURN, H. M. 2005 Three-dimensional instabilities and transition of steady and pulsatile flows in an axisymmetric stenotic tube. *J. Fluid Mech.* **533**, 297–327.